Impact of Receiver Saturation on Surface Doppler Velocity Measurements From the EarthCARE Cloud Profiling Radar

Alessandro Battaglia, *Member, IEEE*, and Pavlos Kollias

Abstract—Antenna-pointing techniques that rely on Earth's surface Doppler velocity measurements are expected to play a crucial role in enabling antenna mispointing corrections in space-borne radar systems. Here, the impact of the EarthCARE cloud profiling radar (CPR) receiver saturation on the quality of the surface Doppler velocity measurements is discussed. The CPR linear receiver is expected to saturate always from surface echoes. Our results based on an I/Q simulation framework show that for the EarthCARE radar configuration: 1) biases introduced by saturation will be negligible; 2) the standard deviation of the velocity estimates will increase by 30–50% when moving from unsaturated to completely saturated surface return for a corresponding pulse repetition frequency in the range between 6.1 and 7.5 kHz. As a consequence longer integration times will be necessary to achieve the same accuracy in presence of complete saturation.

Index Terms—Doppler effect, millimeter wave radar, radar application, radar theory, signal processing, surface saturation.

I. INTRODUCTION

THE joint European Space Agency and Japanese Aerospace Exploration Agency Earth Cloud Aerosol Radiation Explorer (EarthCARE, hereafter EC) mission, scheduled for launch in late 2016, will feature an atmospheric Cloud Profiling Radar (CPR) with Doppler capability, the first-ever in space [1]. Several factors affect the quality of the Doppler measurements from space, and mitigation strategies have been the subject of extensive research in the recent past, including, non-uniform beam filling (e.g., [2]–[5]), Doppler fading due to the platform motion [6], multiple scattering [7], and antenna mispointing [8]. For the latter, it has been suggested that referencing antenna-pointing techniques that rely on the Earth's surface Doppler velocity measurements (e.g., [8], [9]) or on natural targets (e.g., ice clouds, [10]) can be used to mitigate this problem.

In addition to the Earth's surface Doppler velocity, the Earth's surface echo intensity is also of great interest. In the absence of significant multiple scattering [11] and strong pre-
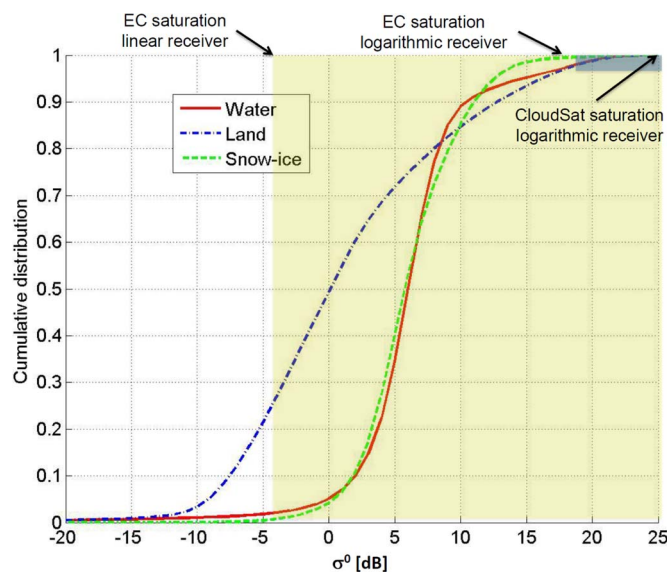
Fig. 1. Cumulative distribution of attenuated σ^0 as derived from CloudSat 1B-CPR product. No attenuation correction is adopted. A full year of CloudSat data (2007) has been used. Yellow (blue) shadowed areas identify regions where the EC logaritmic (linear) receiver is expected to saturate.

cipitation attenuation, the Earth's surface produces the highest CPR returns [12], and its intensity has been used to retrieve the path-integrated attenuation (PIA), a strong constraint in rainfall rate retrievals from space [13]. Two major requirements for the utilization of the Earth's surface echo for PIA estimates are the absence of multiple scattering [11] and the avoidance of the CPR receiver saturation by the surface return. CloudSat is designed to detect weak targets (-30 dBZ sensitivity at nominal operational conditions [12]) and the Earth's surface produces echoes with values peaking at 40–50 dBZ. Thus the requirement to avoid CPR receiver saturation from the Earth's surface requires a radar receiver dynamic range of more than 90 dB considering that we need to digitize the CPR receiver noise as well. Fig. 1 shows the cumulative distribution of the CloudSat CPR attenuated normalized surface backscattering cross sections (σ^0) for different surfaces collected over an entire year of observations (2007). The corresponding pdfs of attenuation-corrected σ^0 for different surface types can also be found in [14]. The CloudSat CPR receiver saturation point is also indicated in Fig. 1. Only a small fraction of surface returns saturates the CPR and thus, the surface return can be used to retrieve the PIA. This is achieved using a standard logarithmic amplifier receiver channel that compresses the amplitude of

strong surface return, the use of a 14-bit A/D converter and by setting the CloudSat CPR to point 0.16° off-nadir to reduce the strength of the surface return from flat specular surfaces (e.g wetlands and shallow waters) [12].

The EC CPR has very similar technical specifications [15] to the CloudSat CPR (e.g., [16]). The EC CPR features a larger antenna than the CloudSat CPR (2.5 m versus 1.85 m) and orbits at lower altitude than the CloudSat CPR (400 km versus 700 km for the CloudSat CPR). The differences in antenna size (2.8 dB gain) and altitude (4.8 dB gain) between the CloudSat and EC CPR will result to an additional gain of approximately 7 dB for the EC CPR. Thus, the EC CPR logarithmic amplifier receiver that measures the received echo power will saturate 7 dB earlier compare to the CloudSat CPR (Fig. 1). Thus, a larger fraction of surface echoes (especially over lakes and wetlands) is expected to saturate the receiver and make the estimation of PIA not possible.

Here, we are concerned with the expected saturation of the EC CPR linear amplifier receiver channel that is used to estimate the Doppler velocity using the I/Q digitized time series. Linear amplifier receivers typically do not compress the amplitude of the return signal, thus saturate much earlier than logarithmic amplifier receivers. In the case of the EC CPR preliminary measurements have demonstrated that the receiver saturation is driven by a clipping-type saturation of the I/Q detector. The linear amplifier receiver is expected to saturate at least 25 dB earlier than the logarithmic receiver (NICT personal communication). Thus, it is expected that the Earth's surface return will almost always saturate the CPR linear receiver. According to Fig. 1 water and snow/ice-covered surfaces— which accounts for 65% and 11% of the surfaces observed by CloudSat—will be saturated for more than 99% of the times while land surfaces (free from snow and ice) will saturate for roughly 75% of the times.

The focus of this work is on the impact of the *clipping-type I/Q signal saturation effect of the linear receiver* on the quality of the Earth's surface Doppler velocity measurements for the EC CPR. It is worth mentioning that there are potentially several mechanisms causing receiver saturation (e.g., related to amplifiers, filters, mixers). The clipping assumption on the type of receiver saturation therefore represents the *fundamental hypothesis* underpinning this work. Some of the key science questions that we would like to address are:

1) what is the effect of receiver saturation on the estimates of Earth's surface Doppler velocity for different levels of the signal above the saturation point?
2) How CPR receiver saturation will affect the use of Earth's surface Doppler referencing techniques for correcting the antenna mispointing?
3) What is the impact for future systems that will employ either larger antennas or higher Pulse Repetition Frequencies (PRF) to mitigate some of the Doppler challenges from space?

To answer these questions an I/Q voltage simulator is used [17]. The saturation is simulated as an amplitude clipping of the I/Q voltages time series at a level determined by the pre-scribed saturation point that determines the CPR linear receiver saturation (Section II). Results are discussed in Section III and conclusions drawn in Section IV.

II. SIMULATION FRAMEWORK

The receiver has two synchronous detectors which detect in-phase I and quadrature-phase Q components of the echo signal V. The resulting signal is usually referred to as complex demodulated, or I/Q-data. According to Euler's relation, the echo voltage can be represented by a 2-D phasor diagram in a complex plane. In the process of generating I and Q voltages, the receiver electronics also add noise to these voltages. Both the noise and the I/Q voltages are Gaussian distributed but with the noise process not correlated in time [18]. Each radar pulse (emitted at a given pulse repetition frequency, PRF) produces a pair of I/Q samples at each range gate (determined by the A/D sampling rate). The sampling rate (PRF) also determines the highest sampled frequency. This is often called Nyquist or folding frequency ($f_{Nyq} = PRF/2$), which is half the sampling frequency of a discrete signal processing system. Using the radar wavelength (λ), we can convert the folding frequency to folding velocity or as often-called Nyquist velocity ($V_{Nyq} = PRF\lambda/4$).

Our simulation framework produces raw radar I/Q time series based on a given Doppler spectrum following a stochastic Fourier methodology proposed by [2]–[19]. The receiver input is the periodogram of the return radar signal, i.e., spectral power densities $\mathcal{P}_S(v_i)$ [mW/(ms^{-1})] for every frequency (velocity) bin v_i [ms^{-1}], provided at a sampling rate several times higher than the actual sampling rate (e.g., PRF) of the spaceborne radar (e.g., by a factor of 5) for a total of n_{fft} spectral points. This procedure avoids velocity folding for typical meteorological targets. Using the total received power $P_S = \sum_i \mathcal{P}_S(v_i)\Delta v$ where Δv is the width of the Doppler velocity bins, and the information about the radar receiver saturation point Rx_{sat} [mW], we can infer if the radar receiver is saturated by the return signal and the amount of excess saturation. The condition for radar receiver saturation is $P_S > Rx_{sat}$. Next step is the addition of the radar receiver noise in the received atmospheric signal. The spectral density of noise is white, thus its mean power is independent of the frequency/velocity of the Doppler spectrum. Thus, the noise spectral density $\mathcal{P}_{N,n_{fft}}$ is provided by the following expression:

$$\mathcal{P}_{N,n_{fft}} \left[\frac{mW}{ms^{-1}} \right] = \frac{P_N}{n_{fft}\Delta v}. \tag{1}$$

Once the mean noise power density is estimated, we add a random fluctuation component following the method described in [17] and the spectral power density of the signal-plus-noise $\mathcal{P}_{S+N,n_{fft}}$ is given by the expression:

$$\mathcal{P}_{S+N,n_{fft}}(i) = \left(\mathcal{P}_{S,n_{fft}}(i) + \mathcal{P}_{N,n_{fft}} \right) \ln \left(x(i) \right) \tag{2}$$

with $i = 1, \ldots n_{fft}$ and where x is a random number uniformly distributed between 0 and 1. By so doing the spectral power density accounts for the noise floor and for the random distribution and reshuffling of the scatterers inside the scattering volume. Note that for surface returns the signal-to-noise ratio is assumed to be much greater than one.

Once the radar receiver noise is added in the frequency domain, the next step is to perform Inverse Fast Fourier Transform (IFFT) of the constructed Doppler spectrum in order to retrieve
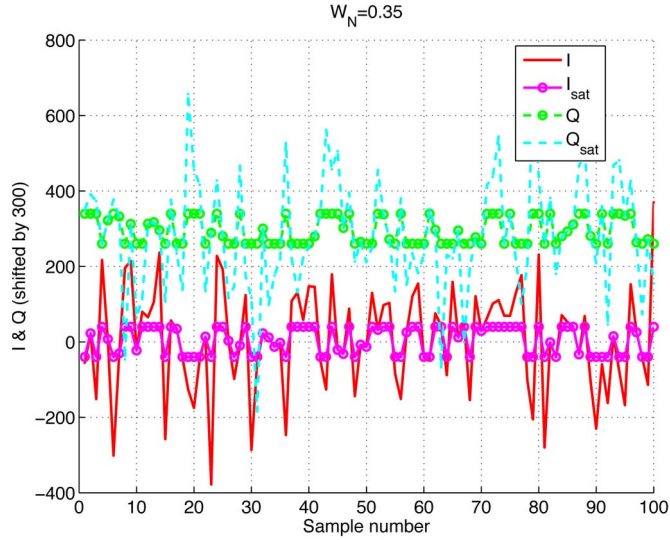
Fig. 2. Example of the effect of clipping onto a 100-element time-series of I and Qs generated for a Doppler Gaussian spectrum with a mean velocity of 1 m/s and with a spectral width of 3.8 m/s sampled at a $PRF = 6800$ Hz. For the saturated sequence the power is 10 dB above the saturation point.

I (in-phase) and Q (quadrature-phase) voltage time series. The IFFT operator is applied to the amplitude spectrum

$$I(t) = Real \left\{ IFFT \left(\sqrt{\mathcal{P}_{S+N,n_{fft}}(i)} e^{j\theta(i)} \right) \right\}$$

$$Q(t) = Imag \left\{ IFFT \left(\sqrt{\mathcal{P}_{S+N,n_{fft}}(i)} e^{j\theta(i)} \right) \right\}$$

θ being a vector of random numbers in $[0, 2\pi]$.

Examples of I/Q time series generated by the IFFT operation are shown in Fig. 2. The successive values of I/Q samples are measured at equally spaced time intervals creating a time-series sequence. If the generated I/Q voltages exceed the maximum allowed voltages $\mathcal{I}_{sat}/\mathcal{Q}_{sat}$ in the I/Q channels of the radar receiver (related to the receiver saturation by $Rx_{sat} = \mathcal{I}_{sat}^2 + \mathcal{Q}_{sat}^2$), hard-clipping of the generated I/Q voltage time series occur (line with circles in Fig. 2).

Hard clipping can produce a variety of effects on the phase of the radar complex signal phasor $C(t) = I(t) + jQ(t)$ as illustrated in Fig. 3.

1) Within the blue square in the center, and along the x and y-axis and the two quadrant secants the phase remains unchanged.
2) Within the four "attractor basins" located at the four corners of the figure (where both I and Q saturate) the complex signal becomes equal to the corresponding "attractor" and the phase assume a constant value of $\Psi_{sat} \equiv \arctan(\mathcal{Q}_{sat}/\mathcal{I}_{sat})$ (top right, yellow quadrant), $180° - \Psi_{sat}$ (top left, purple quadrant), $180° + \Psi_{sat}$ (bottom left, cyan quadrant), $360° - \Psi_{sat}$ (bottom right, red quadrant). In the following we will mainly assume that the same saturation point for the I and Q channel, i.e., $\mathcal{Q}_{sat} = \mathcal{I}_{sat}$. With this assumption $\Psi_{sat} = 45°$.
3) Within the other remaining points (white colored boxes) the complex signals are brought to the perimeter of the blue square and the phase can be either overestimated or underestimated as shown in the two examples.

The simulated I/Q time series are then used to estimate the first three radar Doppler moments (radar reflectivity, mean
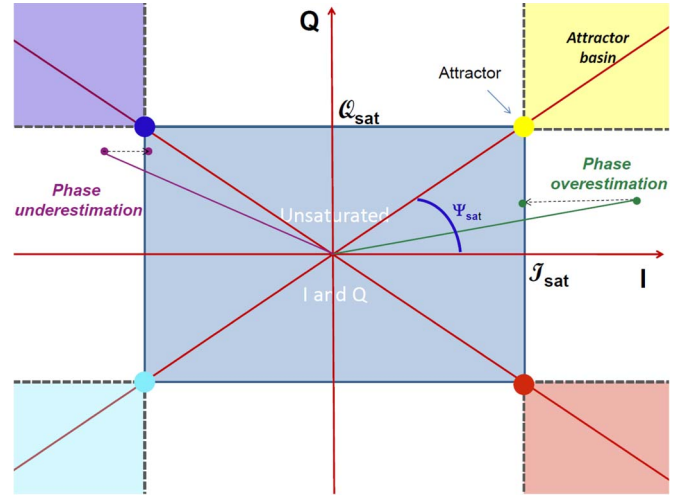

Fig. 3. Effect of hard clipping saturation onto I and Q samples.

Doppler velocity, Doppler spectrum width) using the autocovariance analysis by means of the pulse pair (PP) processing technique [20], [21]. In the autocovariance (time-domain) algorithm, we estimate the autocovariance $R(\tau)$ at lag-one, e.g from pulse to pulse (i.e., τ=Pulse Repetition Time) as [22], [23]

$$\hat{R}(\tau) = \frac{1}{M-1} \sum_{i=1}^{M-1} conj\left(C(t_i)\right) C(t_i + \tau) \quad (3)$$

where M is the number of pulses used for estimating the autocovariance and depends on the adopted PRF and the selected integration time. For any given realization k of the spectral power densities (2) the three radar moments are given by the following expression:

$$\langle P \rangle_{PP}[k] = \hat{R}(0) = \frac{1}{M} \sum_{i=1}^{M} \left(I_i^2 + Q_i^2 \right) \quad (4)$$

$$\langle v_D \rangle_{PP}[k] = \frac{\lambda}{4\pi\tau} \arg\left(\hat{R}(\tau)\right) \quad (5)$$

$$\langle \sigma_D \rangle_{PP}[k] = \frac{\lambda}{2\sqrt{2}\pi\tau} \sqrt{\left| \ln\left(\frac{\hat{R}(0)}{\hat{R}(\tau)} \right) \right|}. \quad (6)$$

Simulating N_R different stochastic realizations of the spectral power densities (2) it is then possible to evaluate the bias and the std of the different moment estimates, e.g., for the Doppler velocity

$$bias_{\langle v_D \rangle_{PP}} = \frac{\sum_{k=1}^{N_R} \langle v_D \rangle_{PP}[k]}{N_R} - v_D \quad (7)$$

$$std_{\langle v_D \rangle_{PP}} = \sqrt{\frac{\sum_{k=1}^{N_R} (\langle v_D \rangle_{PP}[k] - \overline{\langle v_D \rangle_{PP}})^2}{N_R}}. \quad (8)$$

III. RESULTS AND DISCUSSION

A. Case of Complete Saturation

Consider the situation when the signal is much higher than the saturation threshold, *the Doppler spectrum is very narrow*

and the mean Doppler velocity produces a phase shift, ϕ, (always expressed in degrees in the following) with $0° \leq \phi \leq 90°$. In this condition all radar complex signal phasors end up in one of the four attractors while consecutive phasors will be either coincident or will differ by $2\Psi_{sat}$ or by $180° - 2\Psi_{sat}$ (see Fig. 3). The argument of the autocorrelation function in (3) will now be obtained by averaging the contributions of three different types of phasors

$$\langle \phi \rangle_{PP}[deg] = \frac{180°}{\pi} \arg \left[\frac{\phi}{180°} e^{i2\Psi_{sat}} + \frac{\phi}{180°} e^{i(180° - 2\Psi_{sat})} \right.$$
$$\left. + \frac{180° - 2\phi}{180°} e^{i0°} \right]. \quad (9)$$

The results is symmetric for a change $\Psi_{sat} \to 90° - \Psi_{sat}$, i.e., the biases in the Doppler velocities are the same in correspondence to the same level of unbalancing (regardless this is occurring in the I or in the Q channel). The PP estimate therefore differs from the true value ϕ by a bias $\langle \phi \rangle_{PP} - \phi$ and is depicted with gray symbols in Fig. 4 for different levels of unbalance (squares, circles and triangles for 0, 2, 3 dB unbalancing, respectively) for a target producing a phase shift between $0°$ and $90°$ (or, equivalently, with a Doppler velocity between 0 and $V_{Nyq}/2$). The function can then be extended to ϕ outside the interval $[0°, 90°]$. In fact, first, the bias between $90°$ and $180°$ can be obtained by mirroring and swapping sign to the results of the symbol curves with respect to the point $\phi = 90°$ and, then, extended for periodicity outside the $[0°, 180°]$ interval.

In the case of perfect balancing (i.e., $\Psi_{sat} = 45°$) we can conclude that in presence of complete saturation and of very narrow spectra the bias introduced by saturation in PP estimates is zero at integer multiples of $45°$ (corresponding to $\approx \pm V_{Nyq}/4$) and reaches a maximum and a minimum of $\approx \pm 4.1°$ (or in terms of velocities of $\approx \pm V_{Nyq}/44.2$) at $45° \pm 45°\sqrt{(4/\pi) - 1}$ degrees (i.e., circa 21.5 and 68.5° corresponding to $V_{Nyq}/8.37$ and $V_{Nyq}/2.63$). Therefore, velocities between 0 and $V_{Nyq}/4$ will be underestimated while velocities between $V_{Nyq}/4$ and $V_{Nyq}/2$ will be overestimated (and so on with periodicity). With increasing unbalancing the bias is moving from the square into the circle and the triangle curve for a 3 dB (i.e., a factor 2) unbalancing (Fig. 4). In such case the bias reaches a minimum/maximum of amplitude $\approx 8.2°$ ($V_{Nyq}/22$) at around $\pm 30.6°$ ($\pm V_{Nyq}/5.88$).

When the curves corresponding to (9) (gray symbols in Fig. 4) are convolved with a spectrum with large spectral width, the expected effect will be to significantly suppress the bias. Unbalancing between the I and Q channel is expected to increase the standard deviations of the estimates of mean Doppler velocities.

The case of complete saturation but *spectral width larger than zero* can be studied by using the fact that the normalized distribution function of the lag-1 phase difference $\Delta\theta(t) \equiv \theta(t + \tau) - \theta(t)$ of the I/Q is given by [23]

$$f(\Delta\theta(t)) = \frac{1 - \rho^2(\tau)}{2\pi} (1 - \beta^2)^{-\frac{3}{2}}$$
$$\left[\beta \arcsin\beta + \frac{\pi\beta}{2} + \sqrt{1 - \beta^2} \right] \quad (10)$$
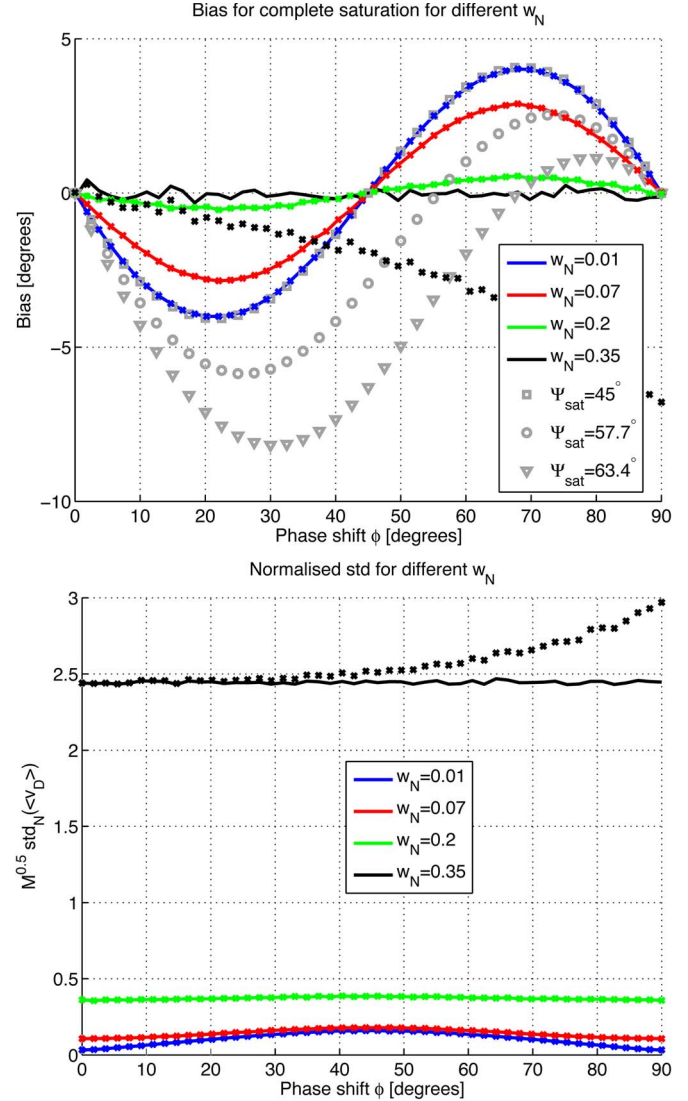

Fig. 4. Pulse-pair biases and normalized standard deviations in presence of complete hard-clipping saturation as a function of the Doppler phase shift for different normalized spectral widths $w_N \equiv (\sigma_D/2V_{Nyq})$. Continuous lines (crosses) correspond to a situation where perfect de-aliasing (no de-aliasing) is applied. The phase shifts maps into the Doppler velocity via the relationship $v_D = V_{Nyq}\phi[deg]/180$. Theoretical biases estimates derived from (9) and corresponding to $w_N = 0$ are shown with gray squares in the top panel. The other gray symbols represents the effect of increasing the unbalancing between I and Q from 0 to 2 (circles) and 3 (triangles) in case of complete saturation.

where $\beta = \rho(\tau)\cos(\Delta\theta - \phi)$ and $\rho(\tau)$ is the magnitude of the correlation coefficient at lag-1, e.g., for a Gaussian spectrum with spectral width, σ_D, $\rho(\tau) = e^{-(8\pi^2/\lambda^2)\sigma_D^2\tau^2}$. In case of complete saturation only the difference in the phases of the received signal between successive pulses is affecting the Doppler velocity estimate (the amplitudes are the same). It is therefore enough to understand how the phase difference distribution described by (10) is mapped into the distribution which is appropriate of clipped I/Qs in case of full saturation. This can be done by generating I/Q phase sequences according to the following procedure.

1) By taking $\theta(t)$ randomly distributed in $[0, 360°]$ and $\Delta\theta(t)$ distributed according to (10) it is possible to create time series of $\theta(t)$ and $\theta(t + \tau) = \theta(t) + \Delta\theta(t)$.
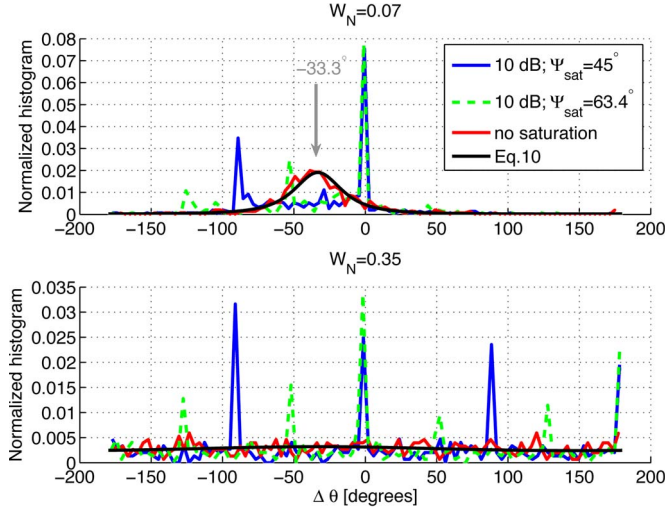
Fig. 5. Distribution of $\Delta\theta$ as derived from an I/Q time series generated according to the procedure described in Section II in absence of saturation (red line) and with a saturation level of 10 dB in presence of perfect balancing (blue line) or with a 3 dB unbalancing between the I and Q channels (green line) for a narrow (top) and an EC-like broad spectrum (bottom panel). The distribution described by (10) is drawn as black line. The assumed mean Doppler velocity is 1 m/s (which corresponds to a phase shift of $-33.3°$ as indicated by the gray arrow) and 433 I/Q samples have been considered, which correspond to an integration length of 500 m and $PRF = 6800$ Hz for the EC-CPR.

2) Then we can use the previously computed time series to convert $\Delta\theta(t)$ into their corresponding saturated values $\Delta\theta_{sat}(t)$ by using the phases of the attractors as shown in Fig. 3.

3) From $\Delta\theta_{sat}(t)$ the correlation at lag-1 can be computed and then the Doppler velocity estimated from (5).

An example of distribution of $\Delta\theta$ with and without accounting for saturation/balancing is shown in Fig. 5 in correspondence to a narrow (top) and an EC-like broad spectrum (bottom panel). The distributions are derived from only 433 I/Q samples. This number corresponds to an integration length of 500 m and a $PRF = 6800$ Hz for the EC-CPR ([4]). The distribution with no saturation corresponds well to the result expected by (10) with the larger normalized spectral width, defined as the Doppler spectral width normalized by the $2V_{Nyq}$ factor ($w_N \equiv (\sigma_D/2V_{Nyq}) = 0.35$) showing a very flat distribution. Saturation radically affects the distribution and its shape, with the appearance of peaks in correspondence to the phase differences between the attractors (roughly in 30% of the cases for a 10-dB saturation level). Note that while in the case of perfect balancing (blue curve) the phase differences between attractors correspond to four points only (0, $\pm90°$ and 180°) in the presence of unbalancing (red dashed curve) the possible phase differences are more numerous (0, $\pm2\Psi_{sat}$ and $\pm180° - 2\Psi_{sat}$, 180°).

In order to understand the effect of different PRFs and spectral widths it is useful to normalize quantities by using as a normalization factor $2V_{Nyq}$ [24]. Results for biases and standard deviations computed according to (7) and (8) are shown in Fig. 4. In the bottom panel the effect of reduced standard deviations with increasing number of samples, M, is compensated for by multiplying by $\sqrt{M}$. Continuous lines (crosses) correspond to a situation where perfect de-aliasing (no de-aliasing) is applied. As expected the biases are significantly

decreasing when increasing the normalized spectral width, w_N, defined as the Doppler spectral width normalized by the $2V_{Nyq}$ factor. At $w_N = 0.01$ the solution is basically spot on with the theoretical expectation at $w_N = 0$ (compare blue line and gray squares) while at $w_N = 0.35$ the bias introduced by saturation has completely disappeared (continuous black line in the top panel). For such a large w_N the bias is indeed dominated by aliasing effects and exceeds 6° for $\phi > 90°$ (i.e., Doppler velocities exceeding $V_{nyq}/2$). The normalized standard deviations ($std_N = std/2V_{Nyq}$) of the Doppler estimates are rapidly deteriorating when increasing w_N and only at small w_N they show a dependence on ϕ with a maximum reached at 45°. Again aliasing effects are visible only for the largest w_N (black curves) and tend to increase the standard deviation of the Doppler velocity.

B. Generic Case

The simulation framework described in Section II can be used to analyze any situation with intermediate levels of the signal above the saturation point (hereafter referred as saturation levels). Two 94 GHz radar configurations are here selected as an example: a PRF typical for EC CPR (6.8 kHz, $V_{Nyq} = 5.4$ m/s) and one very large PRF (34 kHz, $V_{Nyq} = 27.1$ m/s). The large PRF is here introduced to understand the effect of saturation for systems that employ polarization diversity ([15], [25] and reference therein). In such systems the decorrelation is dictated by the distance between the V and H pulses, T_{HV}. This means that for Doppler estimates the "effective" PRF is given by $(1/T_{HV})$. An effective PRF of 34 kHz corresponds to a pulse separation of ~30 μs. In order to avoid second trip echoes H-V pairs are typically transmitted at a much lower frequency. The latter will of course affect the number of useful samples in the pulse-pair processing. A common integration length of 500 m is used (corresponding to $M = 472$ and 2361, respectively, but use the second number cautiously remembering the previous comment!) while a Doppler spectral width $\sigma_D = 3.8$ m/s is assumed which corresponds to $w_N = 0.35$ and $w_N = 0.07$, respectively, for the two selected PRFs. Such a spectral width value corresponds to the Doppler fading induced by the EC satellite motion [in fact for Gaussian circular antennas $\sigma_D = \theta_{3dB}v_{sat}/(4\sqrt{\ln(2)})$ with $v_{sat} = 7.6$ km/s, $\theta_{3dB} = 0.095°$ for the EC CPR] and it is therefore the characteristic value expected for surface returns for the EC CPR in absence of serious non-uniform beam filling effects [2]. Biases and standard errors of the mean Doppler velocity estimates are shown in the top and bottom panels of Fig. 6, respectively. Results are shown only for the interval $0 \leq v_D \leq V_{Nyq}/4$ and can be extended by periodicity (with the assumption that aliasing is accounted for) as discussed in the previous section. The low PRF is basically unbiased (top left panel) while the high PRF shows significant biases (down to -0.4 m/s). As predicted by Fig. 4, for the high PRF case, the maxima and minima of biases are occurring in correspondence to 3.2 m/s ($V_{Nyq}/8.37$) and 10.3 m/s ($V_{Nyq}/2.63$) with unbiased estimates at 0, $\pm V_{Nyq}/4$. The amplitude of the maximum biases (0.4) is lower than the theoretical value expected for narrow spectra, i.e., 0.61 m/s ($= V_{Nyq}/44.2$), and in agreement with values shown in Fig. 4 (red curves correspond to $w_N = 0.07$).
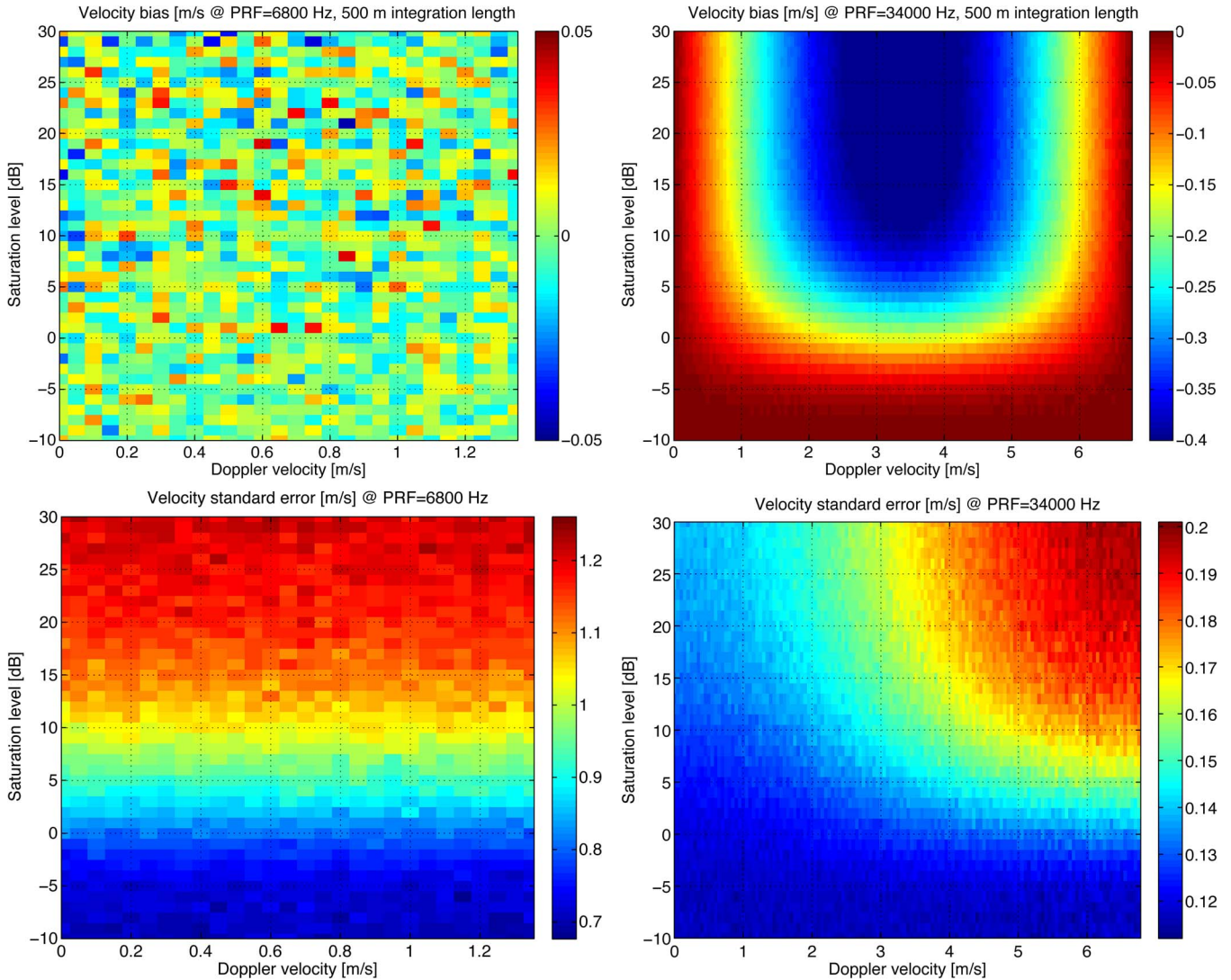
Fig. 6.   Bias (top) and standard error (bottom) of the mean Doppler velocity estimate in m/s at 500 m integration length as a function of the mean Doppler velocity (up to $V_{Nyq}/4$) and of the saturation level for two different PRFs: 6.8 kHz (left) and 34 kHz (right). A Doppler spectral width of 3.8 m/s is used so that the corresponding normalized spectral widths are $w_N = 0.35$ and $w_N = 0.07$, respectively. A positive (negative) bias means velocities are (under)over-estimated by the PP estimates.

In addition to the introduction of biases, saturation also affects the uncertainty of the Doppler estimates. The $std(\langle v_D \rangle_{PP})$ is increasing with the saturation level, reaching basically a plateau for saturation values higher than 20 dB, converging to the values predicted in Fig. 4. While for $w_N = 0.35$ ($PRF = 6.8$ kHz) there is basically no dependence on the Doppler velocity, at $w_N = 0.07$ ($PRF = 34$ kHz) the standard error tends to be worse at Doppler velocities equal $(V_{Nyq}/4)$.

Fig. 7 shows the worst case scenario, i.e., the situation when maximum biases and maximum standard deviations are reached, which corresponds to $v = V_{Nyq}/8.37$ and $v = V_{Nyq}/4$, respectively, for different normalized spectral widths. At low w_N the biases corresponding to large saturation levels (blue dotted and continuous lines) agree with the theoretical prediction of Section III-A with a normalized bias at $w_N = 0$ equal to $1/88.4 = 0.0113$. At small w_N there is a remarkable difference between the unsaturated curve (here represented by the dash-dotted line corresponding to a saturation level equal -10 dB) and the other curves with increasing levels of saturation; with increasing w_N the biases are smoothed out

and for w_N larger than 0.3 there is no difference between the curves with different saturation values. For $w_N > 0.2$ the normalized biases are always lower than 0.2% and therefore negligible for system with low V_{Nyq}. However, when systems with smaller normalized spectral widths are considered (e.g., systems with large antennas and/or employing polarization diversity [15], [25]) such biases cannot be neglected. For instance a polarization diversity 94 GHz radar system with a pulse-pair interval of 20 μs like proposed in [25], [26] is characterized by $v_{Nyq} = 37.5$ m/s; biases up to 0.85 m/s can be produced in presence of full saturation. For completeness the green lines in Fig. 7 correspond to biases expected when $v_D = V_{Nyq}/4$. In such a condition the bias is driven by aliasing effects and is of course increasing with v_D approaching V_{Nyq}.

Similarly to biases, increased levels of saturation cause the standard error of the Doppler velocity estimates to deteriorate (compare red curves in Fig. 7). This deterioration is far less pronounced than that caused by an increase in the Doppler normalized spectral widths. For reference, the Doppler standard error estimated for high SNR (as typically met when
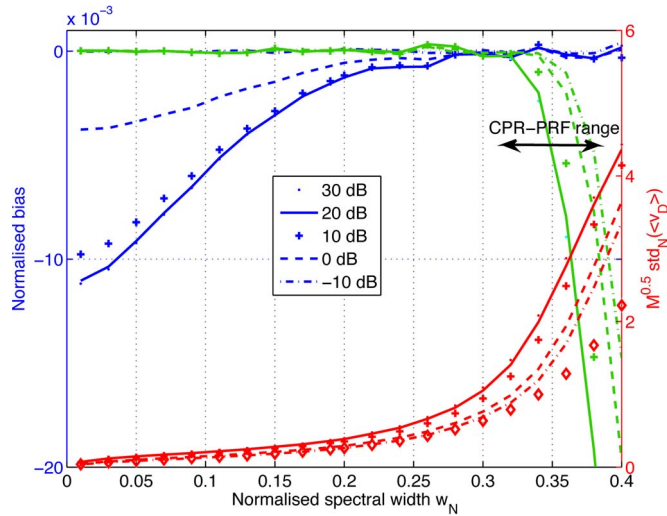
Fig. 7. Normalised bias and normalized standard deviation of Doppler velocity for different saturation levels in correspondence, respectively to $v = V_{Nyq}/8.37$ (blue curves, left y-axis) and to $v = V_{Nyq}/4$ (red curves, right y-axis), i.e., where maximum biases and maximum std are reached. Green curves (left y-axis) correspond to biases for $v = V_{Nyq}/4$ and are shown to demonstrate the effect of aliasing. Red diamonds corresponds to normalized standard deviation of Doppler velocity estimated from perturbation theory in unsaturated conditions (11).
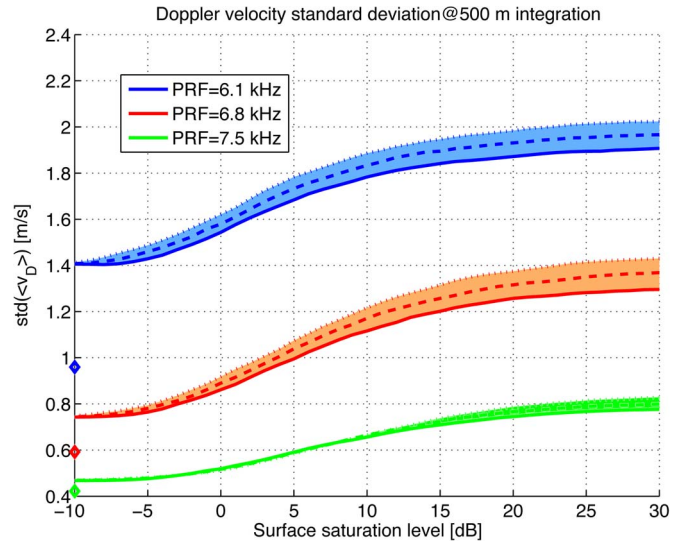

Fig. 8. Standard error of the Doppler velocity estimates for three different EC CPR $PRFs$ as a function of the saturation level with perfect balancing in saturation between I and Qs ($\Psi_{sat} = 45°$). The diamonds are the estimates at high SNR when no saturation effects are assumed as derived from perturbation theory. The shaded area marks the increase in the standard error of the Doppler velocity estimates when there is an increase from perfect balancing (continuous lines), to 2 dB (dashed) and 3 dB (dotted) unbalancing between I and Qs.

considering surface returns) when averaging M samples and in condition of no saturation is given in [20]

$$\sqrt{M}\,\mathrm{std}_N(\langle v_D \rangle) = \sqrt{\frac{w_N}{4\sqrt{\pi}}}\frac{\sqrt{e^{(2\pi w_N)^2} - 1}}{2\pi w_N} \qquad (11)$$

and is plotted as black diamonds in Fig. 7. Results fit well with the -10 dB (unsaturated) curve for $w_N < 0.32$. For larger w_N (11), which is based on perturbation theory, is not valid anymore and is typically underestimating the true standard error of the Doppler velocity estimates.

C. Saturation Effects Expected on Doppler Signal for an EC-Like System

The EC CPR will adopt $PRFs$ in the range between 6.1 and 7.5 kHz corresponding to Nyquist velocities of 4.9 and 6 m/s. By using as before a spectral width $\sigma_D = 3.8$ m/s surface spectra are then characterized by $0.32 < w_N < 0.39$. This means that the bias associated with saturation effects (blue line in Fig. 7) will always be negligible (less thanref 1.5 cm/sec). This guarantees the possibility of using even saturated returns from the surface as a reference target for the Doppler pointing corrections, [8]. It is important to note that accurate Doppler velocity unfolding (when needed) is required before the surface Doppler velocity is used as a reference target. Accurate unfolding of the surface Doppler velocity is possible in areas with minimum non-uniform beam filling conditions (e.g., over ocean in precipitation-free areas).

For the EC configuration Doppler velocity accuracies are detailed in Fig. 8 for three different $PRFs$ in the expected operation range as a function of the saturation level. The continuous lines correspond to a perfect balancing condition ($\Psi_{sat} = 45°$). Roughly speaking the standard deviation in the velocity estimates is increasing by 30–50% when moving from

unsaturated to completely saturated surface return for PRF in the range 6.1–7.5 kHz. As a consequence longer (by a factor in the range between 1.7 and 2.25) integration time will be necessary to achieve the same accuracy in presence of complete saturation. The effect of saturation is however smaller than the drastic change in accuracy occurring when changing the PRF, an effect already noted in [4], [5]. The effect of unbalancing between the I and Q channels is depicted by the shadowing with the dotted (dashed) lines corresponding to an unbalancing of 3(2) dB. As expected an increased level of unbalancing is slightly increasing the Doppler velocity standard deviation. Of course in situations of smaller Doppler spectral widths the unbalancing can be far more damaging. Finally, note that for unsaturated spectra the accuracies as derived from the MonteCarlo simulation exceeds the values (diamonds in Fig. 8) predicted according to perturbation theory [see (11)].

IV. CONCLUSION

Referencing antenna-pointing techniques that rely on Earth's surface Doppler velocity measurements are expected to play a crucial role in enabling antenna mispointing corrections in spaceborne radar systems envisaged in future missions. The EC CPR, the first ever spaceborne cloud radar with Doppler capabilities, is expected to experience saturation in the linear (Doppler) receiver from almost all surface types. By simulating the saturation process as an hard I/Q clipping, which represents the key assumption of this paper, we can draw the following conclusions.

1) Phase biases increase with the saturation level, they are zero for phase shifts that are integer multiples of $45°$ with maxima and minima in between. Biases tend to reduce with increasing normalized Doppler widths, w_N. For the PRF range envisaged for EC they appear to be negligible (i.e., ≤ 2 cm/s) even for complete saturation.

2) Normalized standard deviations of the estimates of mean velocities tend to increase with w_N and with the saturation level. For the EC system standard errors of the Doppler velocity estimates deteriorate by 30–50% for PRF ranging between 6.1 to 7.5 kHZ with saturation levels passing from -10 dB to $+30$ dB. In the latter condition integration lengths 70% and 125% longer are needed to achieve the same error as in the case of unsaturated conditions. The situation is only slightly deteriorated even in presence of large (3 dB) unbalancing between the I and Q channels saturation.

3) Systems with lower w_N or larger Nyquist intervals (like polarization diversity systems) will be prone to non-negligible velocity biases if hard-clipping I/Q receiver saturation occurs. Thus, appropriate technical solutions to mitigate linear receiver saturation should be considered.

REFERENCES

[1] A. J. Illingworth *et al.*, "The EarthCARE satellite: The next step forward in global measurements of clouds, aerosols, precipitation and radiation," *Bull. Amer. Meteorol. Soc.*, to be published.

[2] S. Tanelli, E. Im, S. L. Durden, L. Facheris, and D. Giuli, "The effects of nonuniform beam filling on vertical rainfall velocity measurements with a spaceborne Doppler radar," *J. Atmos. Ocean. Technol.*, vol. 19, no. 7, pp. 1019–1034, Jul. 2002.

[3] N. A. J. Schutgens, "Simulated Doppler radar observations of inhomogeneous clouds: Application to the EarthCARE space mission," *J. Atmos. Ocean. Technol.*, vol. 25, no. 9, pp. 1514–1528, Jan. 2008.

[4] O. Sy *et al.*, "Simulation of EarthCARE spaceborne Doppler radar products using ground-based and airborne data: Effects of aliasing and nonuniform beam filling," *IEEE Trans. Geosci. Remote Sens.*, vol. 52, no. 2, pp. 1463–1473, Feb. 2014.

[5] P. Kollias, S. Tanelli, A. Battaglia, and A. Tatarevic, "Evaluation of EarthCARE cloud profiling radar Doppler velocity measurements in particle sedimentation regimes," *J. Atmos. Ocean. Technol.*, vol. 31, no. 2, pp. 366–386, Feb. 2014.

[6] P. Amayenc, J. Testud, and M. Marzoug, "Proposal for a spaceborne dual-beam rain radar with Doppler capability," *J. Atmos. Ocean. Technol.*, vol. 10, no. 3, pp. 262–276, Jun. 1993.

[7] A. Battaglia, T. Augustynek, S. Tanelli, and P. Kollias, "Multiple scattering identification in spaceborne W-band radar measurements of deep convective cores," *J. Geophys. Res.*, vol. 116, no. D19, pp. D19201-1–D19201-12, Oct. 2011.

[8] S. Tanelli, E. Im, S. R. Mascelloni, and L. Facheris, "Spaceborne Doppler radar measurements of rainfall: Correction of errors induced by pointing uncertainties," *J. Atmos. Ocean. Technol.*, vol. 22, no. 11, pp. 1676–1690, Nov. 2005.

[9] J. Testud, P. H. Hildebrand, and W.-C. Lee, "A procedure to correct airborne Doppler radar data for navigation errors using the echo returned from the Earth's surface rainfall-rate," *J. Atmos. Ocean. Technol.*, vol. 12, no. 4, pp. 800–819, Aug. 1995.

[10] A. Battaglia and P. Kollias, "Using ice clouds for mitigating the Earth-CARE Doppler radar mispointing," *IEEE Trans. Geosci. Remote Sens.*, to be published.

[11] A. Battaglia, J. M. Haynes, T. L'Ecuyer, and C. Simmer, "Identifying multiple-scattering affected profiles in CloudSat observations over the Oceans," *J. Geophys. Res.*, vol. 113, no. D8, pp. D00A17-1–D00A17-13, Apr. 2008.

[12] S. Tanelli *et al.*, "CloudSat's cloud profiling radar after 2 years in orbit: Performance, calibration, processing," *IEEE Trans. Geosci. Remote Sens.*, vol. 46, no. 11, pp. 3560–3573, Nov. 2008.

[13] J. M. Haynes *et al.*, "Rainfall retrieval over the ocean with spaceborne W-band radar," *J. Geophys. Res.*, vol. 114, no. D8, pp. D00A22-1–D00A22-18, Apr. 2009.

[14] C. Mitrescu, T. L'Ecuyer, J. Haynes, S. Miller, and J. Turk, "CloudSat precipitation profiling algorithm-model description," *J. Appl. Meteorol. Climatol.*, vol. 49, no. 5, pp. 991–1003, May 2010, DOI: http://dx.doi.org/10.1175/2009JAMC2181.1.

[15] S. Kobayashi, H. Kumagai, and H. Kuroiwa, "A proposal of pulse-pair Doppler operation on a spaceborne cloud-profiling radar in the W band," *J. Atmos. Ocean. Technol.*, vol. 19, no. 9, pp. 1294–1306, Sep. 2002.

[16] G. L. Stephens *et al.*, "The CLOUDSAT mission and the A-train," *Bull. Amer. Meteorol. Soc.*, vol. 83, no. 12, pp. 1771–1790, Dec. 2002.

[17] D. S. Zrnic, "Simulation of weatherlike Doppler spectra and signal," *J. Appl. Meteorol.*, vol. 14, no. 4, pp. 619–620, Jun. 1975.

[18] E. E. Clothiaux *et al.*, "An evaluation of a 94-GHz radar for remote sensing of cloud properties," *J. Atmos. Ocean. Technol.*, vol. 12, no. 2, pp. 201–229, Apr. 1995.

[19] D. Sirmans and B. Bumgamer, "Numerical comparison of five mean frequency estimators," *J. Appl. Meteorol.*, vol. 14, no. 6, pp. 991–1003, Sep. 1975.

[20] D. S. Zrnic, "Spectral moment estimates from correlated pulse pairs," *IEEE Trans. Aerosp. Electron. Syst.*, vol. AES-13, no. 4, pp. 344–354, Jul. 1977.

[21] D. S. Zrnic, "Estimation of spectral moments for weather echoes," *IEEE Trans. Geosci. Electron.*, vol. GE-17, no. 4, pp. 113–128, Oct. 1979.

[22] R. J. Doviak and D. S. Zrnić, *Doppler Radar and Weather Observations*. Orlando, FL, USA: Academic, 1984.

[23] V. N. Bringi and V. Chandrasekar, *Polarimetric Doppler Weather Radar, Principles and Applications*. Cambridge, U.K.: Cambridge Univ. Press, 2001, p. 266.

[24] S. Tanelli, E. Im, L. Facheris, and E. A. Smith, "DFT-based spectral moment estimators for spaceborne Doppler precipitation radar," in *Proc. SPIE Symp. Remote Sens. Atmos., Environ. Space*, Hangzhou, China, 2002, vol. 4894, pp. 218–229.

[25] A. Battaglia, S. Tanelli, and P. Kollias, "Polarization diversity for millimeter space-borne Doppler radars: An answer for observing deep convection?" *J. Atmos. Ocean. Technol.*, vol. 30, no. 12, pp. 2768–2787, Dec. 2013, DOI: http://dx.doi.org/10.1175/JTECH-D-13-00085.1.

[26] A. Battaglia and P. Kollias, "Doppler performance assessment of a spaceborne cloud stereo-radar concept for a hurricane system," *J. Atmos. Ocean. Technol.*, to be published.

Alessandro Battaglia (M'14) received the Master's degree from the University of Padova, Padova, Italy, with a thesis on particle physics and the Ph.D. degree in physics with the University of Ferrara, Ferrara, Italy.

He is currently a Reader with the Department of Physics and Astronomy, University of Leicester, Leicester, U.K. He is experienced in theoretical research in spaceborne radars, in scattering computations by populations of nonspherical particles, and in microwave radiative transfer in clouds and precipitation.

Pavlos Kollias was born in Athens, Greece, in 1971. He received the B.Sc. and M.Sc. degrees in physics and environmental physics from the University of Athens, Athens, Greece, in 1994 and 1996, respectively, and the Ph.D. degree in meteorology from the University of Miami, Coral Gables, FL, USA, in 2000.

He is currently an Associate Professor and a Canada Research Chair in radar application in weather and climate research with the Department of Atmospheric and Oceanic Sciences, McGill University, Montreal, QC, Canada. He is an international leader in the application of short-wavelength radars for cloud and precipitation research from ground-based and space-based platforms. He is the author of over 70 scientific articles in peer-reviewed literature in the areas of millimeter-wavelength radar research and cloud and precipitation physics. He is a member of the Mission Advisory Group and algorithm development team of the European Space Agency Earth Clouds Aerosols Radiation Experiment (EARTHCARE) Explorer Mission. He is also the leader of the DOE Atmospheric Systems Research (ASR) Radar Science Group.